

# A Preliminary Jupiter Model

W. B. Hubbard

*Lunar and Planetary Laboratory, The University of Arizona, Tucson, AZ 85721, USA.*

and

B. Militzer

*Department of Earth and Planetary Science, Department of Astronomy, University of California, Berkeley, CA 94720, USA.*

## ABSTRACT

In anticipation of new observational results for Jupiter’s axial moment of inertia and gravitational zonal harmonic coefficients from the forthcoming *Juno* orbiter, we present a number of preliminary Jupiter interior models. We combine results from *ab initio* computer simulations of hydrogen-helium mixtures, including immiscibility calculations, with a new nonperturbative calculation of Jupiter’s zonal harmonic coefficients, to derive a self-consistent model for the planet’s external gravity and moment of inertia. We assume helium rain modified the interior temperature and composition profiles. Our calculation predicts zonal harmonic values to which measurements can be compared. Although some models fit the observed (pre-*Juno*) second- and fourth-order zonal harmonics to within their error bars, our preferred reference model predicts a fourth-order zonal harmonic whose absolute value lies above the pre-*Juno* error bars. This model has a dense core of about 12 Earth masses, and a hydrogen-helium-rich envelope with approximately 3 times solar metallicity.

*Subject headings:* equation of state, hydrogen-helium mixtures, ab initio simulations, giant planets, extrasolar planets

## 1. Introduction

In July 2016, the *Juno* spacecraft will enter a bound orbit around Jupiter, and then complete  $\sim 30$  further low-periapse orbits over a period of approximately one

year. Measurements of the spacecraft’s accelerations may reach a precision of  $\sim 1 \mu\text{gal}$  (Kaspi et al. 2010), allowing determination of Jupiter’s external gravitational potential,  $V$ , to a relative precision approaching  $\sim 10^{-9}$ . In roughly the same

time frame, the *Cassini* spacecraft will execute  $\sim 22$  low-periapse orbits around Saturn, making similar measurements of Saturn’s external gravity potential. The non-spherical components of  $V$  provide information about a planet’s interior mass distribution.

In this paper, we construct static interior models intended to represent the present state of Jupiter, using a pressure-density relation  $P(\rho)$  derived from DFT-MD theory for the equation of state of the primary constituent of Jupiter and Saturn, a mixture of hydrogen and helium; see Militzer & Hubbard (2013) and Militzer (2013). This barotrope is used to calculate the zonal harmonic coefficients  $J_{2n}$ , making various assumptions about the interior temperature distribution and core mass. Physically-motivated adjustments of the barotrope are made to achieve agreement with the observed  $J_2$  (Table 1) and discrepancies with currently-observed higher  $J_{2n}$  are discussed. Lines 2-11 of Table 1 give calculated values from interior models discussed in Section 4.

To obtain a barotrope, we start with the grid of *ab initio* adiabats derived in Militzer (2013) and Militzer & Hubbard (2013). These adiabats were determined with density functional molecular dynamics (DFT-MD) simulations using the Perdew-Burke-Ernzerhof (PBE) functional (Perdew et al. 1996) in combination with a thermodynamic integration (TDI) technique to determine the full, nonideal entropy. The simulation cells contained a mixture of  $N_{\text{He}}=18$  helium and  $N_{\text{H}}=220$  hydrogen atoms, corresponding to a helium mass fraction of  $Y=0.245$ , close to the solar value. As discussed in Militzer & Hubbard

(2013), each adiabat is characterized by the value of its absolute entropy per electron,  $S/k_B/N_e$ , where  $k_B$  is Boltzmann’s constant and  $N_e$  is the number of electrons. Hereafter we denote this quantity with the simpler symbol  $S$ .

Recently Becker et al. (2014) constructed Jupiter models based on equations of state that were also derived with DFT-MD simulations but their approach differs in two respects. Becker *et al.* performed simulations for hydrogen and helium separately and then evoked the ideal mixing assumption while we simulated an interacting hydrogen-helium mixture directly. While we computed the full, non-ideal entropy with TDI, Becker *et al.* obtained the entropy indirectly by fitting the internal energy and pressure, which are available in standard DFT-MD simulations. Becker et al. (2014) reported deviations between 4 and 9% when they compared their EOS with Militzer & Hubbard (2013). Such deviations could have a significant repercussion on values of zonal harmonics for interior models.

In this paper, we use the term “entropy” and the symbol  $S$  as a proxy for an adiabatic temperature  $T$  vs. pressure  $P$  relation for the fixed-composition mixture of H and He only (He mass fraction  $Y_0 = 0.245$ ), as determined by our detailed DFT-MD simulations. The simulations give the absolute entropy and other dependent variables as a function of  $T$  and  $P$ , for this specific composition. As discussed in Section 3 below, for the purpose of calculating general pressure-density relations, the same  $T(P)$  relation is taken to apply to adiabats with small, constant perturbations to the composition of the simu-

lations. Moreover, the  $S$  of the outermost layers of the model is determined by requiring a match to the Galileo Probe measurements of  $T(P)$ ; see Figure 5. The corresponding adiabat from our simulations has  $S = 7.08$ . Now, if we perturb this composition by changing  $Y$  and increasing  $Z$ , how might the adiabatic  $T(P)$  change, for  $P > 20$  bar, and how might this affect the barotrope? Let the Grüneisen parameter  $\gamma = (\rho/T)(\partial T/\partial \rho)_S$ , where  $\rho$  is the mass density. Suppose we have a compositional perturbation to  $Y$  and/or  $Z$ , of the order of  $\sim 0.01$ . This might lead to a perturbation  $\Delta\gamma \sim 0.01$ . Over a density range of three orders of magnitude, roughly spanning the jovian mantle, this value  $\Delta\gamma$  would imply a cumulative change of temperature of  $\sim 7\%$ , with respect to the baseline  $T(P)$ . According to Mie-Grüneisen theory (Zharkov & Trubitsyn 1978), the thermal pressure makes up only 10% of the total pressure in the relevant Jupiter layers. Therefore, we expect the fractional change in density to be on the order of  $\sim 0.1 \times 0.01 = 0.001$ . This amount is so small that it is unlikely to affect any of our model predictions. It is certainly smaller than the previously-mentioned 4 to 9% discrepancy with Becker et al. (2014).

Our *ab initio* calculations show that under jovian interior conditions, there is no distinct phase transition from molecular (diatomic, insulating) hydrogen to metallic (monatomic, conducting) hydrogen (Vorberger et al. 2007). However, for convenience in this paper, the term “molecular” layer means layers at pressures below 1 Mbar, where the hydrogen is mostly diatomic. Likewise, the term “metallic” layer means layers at pressures

above  $\sim 2$  Mbar, but still external to a central dense core.

By combining our *ab initio* calculations for Jupiter’s interior adiabat (Militzer 2013) with the *ab initio* hydrogen-helium immiscibility calculations by Morales et al. (2013), we predict that helium rain occurs in Jupiter’s interior. While the detailed physics and dynamics of helium rain is not yet understood, we make the assumption that this process introduces a superadiabatic temperature gradient and a compositional difference between the outer, molecular layer and inner, metallic layer. In our models, the  $T(P)$  of the molecular layer is set by the measurements of the Galileo entry probe while the  $T(P)$  of the metallic layer is a free parameter that we can adjust between two limits. The value of  $S$  labeling  $T(P)$  for the metallic layer cannot be too high because otherwise no helium rain would have occurred in Jupiter according to DFT-MD simulations. The value of  $S$  labeling  $T(P)$  cannot be below the Galileo value because, we assume, the cooling of the metallic layer is less efficient. The assumption of reduced cooling of the metallic layer is consistent with specific models constructed by Nettelmann et al. (2015) who studied the evolution of jovian interior temperature profiles under the influence of H/He demixing and layered double diffusive convection (see upper left-hand panel of Figure 10 of that paper).

For the molecular layer, we assume the helium abundance that was measured by the Galileo probe (von Zahn et al. 1998; Mahaffy et al. 2000). We derive the helium contents in the metallic layer by assuming the planet as a whole has a protosolar helium abundance (Lodders 2003). The dis-

tribution of heavier elements throughout the planet is not well understood. The capture of comets has enriched the envelope over time. Similarly the erosion of the core may have added icy and rocky materials to the envelope (Wilson & Militzer 2012a,b; Wahl et al. 2013; Gonzalez-Cataldo et al. 2014). Given these uncertainties, we introduce three model parameters: the mass of today’s dense core, the heavy element (“metals”) mass fraction in the molecular layer and that in the metallic layer. We assume that both layers are homogeneous and interpolate between both compositions to derive an estimate for the structure of the helium rain layer. Model predictions are not sensitive to details of this procedure because, in Jupiter, the interpolation layer between 1 and 2 Mbar contains very little mass.

This article is organized as follows. In Section 2, we describe how we deal with hydrogen-helium immiscibility. In Section 3, we discuss how one perturbs the helium abundance in a particular EOS and how heavy elements are introduced. In Section 4, we discuss the EOS of different planetary ices and present results from additional *ab initio* simulations. In Section 5, we introduce our reference Jupiter model and discuss variations from it. Before we conclude, we describe in Section 6 how the moment of inertia is derived from CMS theory. In the Appendix, we provide additional details about the CMS calculations.

## 2. Adiabats and Hydrogen-Helium Immiscibility

Figure 1 shows a plot of temperature,  $T$ , versus pressure,  $P$ , for a family of such adiabats as well as the hydrogen-

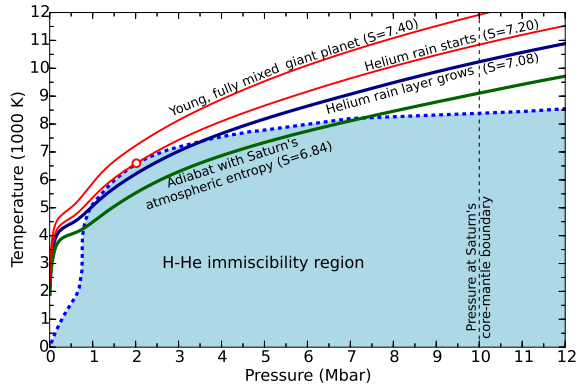


Fig. 1.— General view of effect of immiscibility on Jupiter (and Saturn) evolution. The top two curves are DFT-MD adiabats with relatively high entropy per electron. The adiabat for  $S \approx 7.20$  osculates the boundary of the region of H-He immiscibility, while the adiabat just below it has  $S = 7.08$ , which yields a temperature vs. pressure relation in the Jovian troposphere that matches corresponding data from the Galileo Probe (Seiff et al. 1998). The lowest adiabat has  $S = 6.84$ , which yields a temperature vs. pressure relation that roughly matches Saturn’s tropospheric profile (Lindal et al. 1985). The pressure at Jupiter’s core-mantle boundary (about 40 Mbar) is not shown on this figure.

helium immiscibility domain derived from *ab initio* simulations by Morales et al. (2013). These simulations also used the DFT-MD technique in combination with the PBE functional and TDI method to compute the entropy. They are thus fully compatible with the adiabat from Militzer & Hubbard (2013). As is evident in Figure 1, the interiors of both Jupiter and Saturn enter a region at a pressure  $\sim 1$  Mbar where helium in solar proportion to hydrogen becomes immiscible. Both planets are thus likely to have layers with helium rain. Figure 2 depicts the location of this layer in Jupiter. This prediction is a direct consequence of combining the *ab initio* immiscibility and adiabat calculations with measurements of the planets' tropospheric  $T$  vs.  $P$  profiles (Seiff et al. 1998; Lindal et al. 1985). No temperature or pressure adjustments of the immiscibility domain were needed.

Heavy elements were not considered in this analysis. Depending on the concentration, a small correction to the adiabatic profile would be plausible. We also note that Morales et al. (2013) performed the immiscibility calculations for  $Y = 0.25$  which differs slightly from the protosolar value. However, this concentration difference does not change the immiscibility temperature to a significant degree. Based on the analysis in Nettelmann et al. (2015), we estimate this correction to be of the order 160 K only.

The hydrogen-helium immiscibility hypothesis was first invoked to explain Saturn's luminosity excess (Stevenson & Salpeter 1977a,b). In the immiscibility layer, helium droplets would form and rain down into the deeper interior, resulting in a grad-

ual removal of helium from the planets outer layer. The associated release of gravitational energy provides an energy source to explain Saturn's luminosity excess.

Whether helium rain occurs on Jupiter is less certain. Its interior is hotter and no helium rain is needed to explain its present luminosity (Fortney & Hubbard 2004). The Galileo entry probe measured a small helium depletion in Jupiter's upper atmosphere (0.234 by mass compared to 0.274, the protosolar value (Lodders 2003). Perhaps the strongest evidence for helium rain to occur on this planet comes from the depletion of neon. The Galileo measurements showed that there is ten times less neon in Jupiter's atmosphere compared to solar values. Wilson & Militzer (2010) demonstrated with *ab initio* simulations that neon has a strong preference for dissolving in the forming helium droplets. This offered an explanation for the neon depletion and provided strong, though indirect evidence for helium rain to occur on Jupiter.

According to the more recent *ab initio* calculations, the present Jupiter would encounter the immiscibility domain at pressures above  $\sim 0.9$  Mbar (Figure 1). In Saturn, the domain is entered at  $P \sim 0.8$  Mbar. If a cooling scenario for Jupiter or Saturn involves a steady decrease of entropy with time, then the onset of helium rain would occur when the interior adiabat first touches the boundary of the helium immiscibility domain. The curvature of the boundary is such that a H-He adiabat with  $S \approx 7.20$  osculates the boundary at  $P \sim 2$  Mbar and  $T \sim 6600$  K.

We are thus faced with the task of deriving a barotrope  $P(\rho)$  for present-day

Jupiter which is consistent with the properties of dense, hot hydrogen-helium mixtures shown in Figure 1 and with Jupiter’s presumed cooling history. A detailed, dynamical calculation of the process of helium rain and subsequent evolution of Jupiter’s interior temperature profile is beyond the scope of the present paper, whose aim is to infer a jovian barotrope based on current knowledge of Jupiter’s composition and thermal state, and on current results from *ab initio* simulations of hydrogen-helium mixtures at high pressure. The resulting barotrope is used here to predict Jupiter’s higher zonal harmonic coefficients, whose values are to be measured by *Juno*.

Thus, we make the simplifying assumption that the cooling of early Jupiter to an interior adiabat  $S \approx 7.20$ , corresponding the onset of immiscibility, then leads to reduced heat transport in the region around  $P \geq 2$  Mbar, effectively slowing interior temperature decline, while layers at lower pressures continue to transfer heat to Jupiter’s atmosphere. In this scenario, the present-day Jupiter barotrope for pressures  $\leq 1$  Mbar lies on the Galileo Probe adiabat with reduced He abundance, but at somewhat higher pressures, temperatures follow a higher-entropy adiabat with a slightly-above protosolar helium abundance,  $Y = 0.28$ . The interior adiabat would be expected to lie between  $S \approx 7.20$  (for no heat transport across the immiscibility region) and  $S \approx 7.08$  (for efficient heat transport across the immiscibility region). In the study that we present here, our preferred model has an interior adiabat with  $S = 7.13$  (shown as a heavy line in Figure 3). We refer to this model as

Model DFT-MD 7.13; Its parameters are shown in boldface in Table 1. The  $P(\rho)$  barotrope for Model DFT-MD 7.13 shown in Figure 4. The corresponding  $T(\rho)$  profile is shown in Figure 5.

### 3. Compositional Perturbations to Equation of State

In order to derive general barotropes, we must now evaluate the effects of (1) varying He concentration, and (2) varying metallicity. The barotrope shown in Figures 4 and 5 corresponds to an initial He mass fraction  $Y_0 = 0.245$  and metals mass fraction  $Z_0 = 0$ . Since this composition is a good initial approximation to the Jupiter envelope, we use a perturbation approach to derive the effects of compositional changes. Let the reference barotrope for  $Y_0 = 0.245$  and  $Z_0 = 0$  be  $\rho_0(P)$ . Although this barotrope is computed with detailed DFT-MD simulations not assuming an ideal mixture of H and He, to simplify this derivation we approximate it by an additive volume law,  $V_{\text{H-He}}(P, T) = V_{\text{H}}(P, T) + V_{\text{He}}(P, T)$ , valid for a noninteracting mixture:

$$\frac{1}{\rho_0} = \frac{X_0}{\rho_{\text{H}}} + \frac{Y_0}{\rho_{\text{He}}}, \quad (1)$$

where  $X_0 = 1 - Y_0 = 0.755$ . We now want to change the abundance of helium to  $Y$  and metals to  $Z$ . We assume that the temperature-pressure relation  $T(P)$  is unchanged under perturbations to the composition (i.e., the perturbing admixture is chemically and thermodynamically inert). With this assumption and the additive volumes approximation,  $V_{\text{H-He-Z}} = V_{\text{H}} + V_{\text{He}} + V_{\text{Z}}$ , the perturbed density is

given by,

$$\frac{1}{\rho} = \frac{1 - Y - Z}{\rho_H} + \frac{Y}{\rho_{He}} + \frac{Z}{\rho_Z}, \quad (2)$$

where  $V_Z$  and  $\rho_Z$  is the volume and density of the metals component. Rewriting Equations (1) and (2), we find

$$\frac{\rho_0}{\rho} = \frac{1 - Y - Z}{1 - Y_0} + \frac{ZY_0 + Y - Y_0}{1 - Y_0} \frac{\rho_0}{\rho_{He}} + Z \frac{\rho_0}{\rho_Z}, \quad (3)$$

with all densities evaluated for the reference  $T(P)$ . The same equation is obtained if one starts from a fully interacting hydrogen-helium equation of state and then perturbs the helium and metals abundances.

For the composition in Jupiter’s outer layers, at  $P < 1$  Mbar, we adopt abundances from Galileo Probe measurements (Wong et al. 2004). In this region the main contributors to  $Z$  are the molecules  $\text{CH}_4$  and  $\text{NH}_3$ , and for the  $\text{H}_2\text{O}$  abundance we adopt the largest value measured by the probe (rather than assuming a solar abundance for  $\text{H}_2\text{O}$ ). Neglecting other metals, we obtain  $X = 0.7498$ ,  $Y = 0.2333$ ,  $Z \approx 0.0169$ , for the presumed jovian composition at layers with  $P < 1$  Mbar.

Using a DFT-MD equation of state for pure He (Militzer 2008) along the  $T(P)$  shown in Figure 5, we obtain the density-pressure relation shown in Figure 6.

#### 4. Equation of State of $\text{H}_2\text{O}$ , $\text{CH}_4$ , and $\text{NH}_3$

Evaluation of the perturbation term  $\rho_0/\rho_Z$  in Eq.(3) is somewhat more complex because of the presence of multiple molecular species, but need not be highly precise because the contribution of this term is

comparatively small. We continue to assume, for pressures above and below the He-immiscibility gap, that the main contributors to the  $Z$  mass fraction are the molecules  $\text{H}_2\text{O}$ ,  $\text{CH}_4$ , and  $\text{NH}_3$ , in solar proportions. Thus, to evaluate  $\rho_0/\rho_Z$ , it is necessary to evaluate the density change of these molecular entities along the jovian  $T(P)$ . We thus performed a number of DFT-MD simulations of  $\text{H}_2\text{O}$ ,  $\text{CH}_4$ , and  $\text{NH}_3$  under such conditions.

All simulations were performed with the VASP code (Kresse & Furthmüller 1996) using the PBE functional. Pseudopotentials of the projector-augmented wave type (Blöchl 1994) and a plane wave basis set cutoff of 1100 eV were employed. The zone-average point,  $k = (\frac{1}{4}, \frac{1}{4}, \frac{1}{4})$ , was used to sample the Brillouin zone. A time step of 0.2 fs was used. Density, temperature, and composition were prescribed in the simulations. After an initial equilibration period, the pressure was derived by averaging over the MD simulation.

We first benchmarked our simulations by comparing our results with the shock wave measurements by Nellis et al. (1997) that compressed a mixture of water, ammonia, and isopropanol ( $\text{C}_3\text{H}_8\text{O}$ ) to 200 GPa. This mixture, labeled “synthetic Uranus”, was designed to resemble the different planetary ices in the outer solar system. The concentrations of the heavy nuclei (C:O=0.529, N:O=0.162) indeed closely resemble solar proportions. However, the mixtures is somewhat depleted in hydrogen (H:O=3.54) while one would expect a H:O ratio of 4.60 if one mixes  $\text{H}_2\text{O}$ ,  $\text{CH}_4$ , and  $\text{NH}_3$  in O:C:N proportions that were used in the experiments. This difference prompted us to

perform two sets of simulations. First we studied a hydrogen-depleted mixture, H:O:C:N=87:25:13:4, that closely resembles the “synthetic Uranus” mixture within the size constraints of typical simulations that accommodate between 100 and 200 atoms.

Our simulation results in Table 2 show excellent agreement with the experimental findings. It should be noted that if we prescribe the central values for densities and temperature, that were measured in the experiments, then our computed pressures were, respectively, slightly higher and slightly lower than those reported in the experiments. However, if we adjusted the density and temperatures in our simulations within the experimental  $1\sigma$  uncertainties then our computed pressures fall within the experimental error bars of the two available measurements. This provides another example for DFT-MD simulations that closely reproduce experimental findings (Knudson et al. 2012).

In Table 2, we also report results from simulations of a H:O:C:N=99:21:12:3 mixture that exactly represent the hydrogen contents of a solar H<sub>2</sub>O, CH<sub>4</sub>, and NH<sub>3</sub> mixture. Because of the higher hydrogen content, the density is lower than that of “synthetic Uranus” when compared for the same  $P$  and  $T$ . The simulation results were incorporated into Figures 7 and 8.

Figure 7 shows calculations used to perform the estimation of  $\rho_0/\rho_Z$ . In the low-pressure region of this figure, pressure-density values for CH<sub>4</sub>, NH<sub>3</sub>, and H<sub>2</sub>O are combined assuming ideal mixing. In the lower left-hand part of this figure, orange dots show the ideal-gas partial pressure of an ideal mixture of the three

molecules along the jovian  $T(P)$ , with virial corrections up to  $P \sim 2$  Kbar. Dash-dot curves at the top of the figure show zero-temperature  $\rho(P)$  relations calculated from quantum-statistical models and tabulated in Zharkov & Trubitsyn (1978). The orange dashed curve shows the resulting zero-temperature  $\rho(P)$  relation for a solar mixture of the three molecules. Dots in the upper right-hand corner of this figure show finite-temperature calculations for pressures greater than a megabar; Figure 8 shows a zoom of this region, along with experimental data points for “synthetic Uranus” (Nellis et al. 1997).

To construct  $\rho_Z(P)$  in the gap between low pressure and high pressure, we perform a linear interpolation in log-log space as indicated in Figure 7.

Figure 9 shows  $\rho_0/\rho_Z$  (dashed curve) for assumed Galileo Probe composition (for pressures below 2 Mbar). As a hypothesis to be tested by our preliminary Jupiter model, we assume that all jovian layers at pressures less than  $\sim 1$  Mbar have the composition measured by the Galileo Probe, with a corresponding correction to the density given by Equation (3). In this pressure range, we find from Figure 6 and Figure 9 that  $\rho_0/\rho_{He} \approx 0.48$  and  $\rho_0/\rho_Z \approx 0.38$ , leading to  $\rho_0/\rho = 0.995$ . The latter number is fortuitously close to unity because the slightly lower Galileo Probe He abundance (relative to the DFT-MD simulations) is almost compensated by the presence of metals.

Note that H<sub>2</sub>O is depleted relative to CH<sub>4</sub> and NH<sub>3</sub> in the Galileo Probe data. That is, Galileo Probe data show H<sub>2</sub>O approaching a solar ratio to hydrogen-helium, while CH<sub>4</sub> and NH<sub>3</sub> are approximately

three times their solar ratio to hydrogen-helium.

In contrast, for solar proportions of  $\text{CH}_4:\text{NH}_3:\text{H}_2\text{O}$  and for  $P > 1$  Mbar, we have  $\rho_0/\rho_Z > 0.38$ , and  $\rho_0/\rho_Z \approx 0.42$  through the bulk of the jovian envelope (Figure 9, solid curve).

For layers at pressures greater than 2.7 Mbar, we take the He and metals abundances to be slightly higher than the protosolar values  $Y = 0.2741$  and  $Z = 0.0149$  (Lodders 2003). Our DFT-MD equation of state, combined with the constraints of Jupiter’s total mass, volume, and  $J_2$  and any reasonable interior temperature distribution, does not imply a large increase of  $Z$  above its protosolar value, for otherwise the densities would be too large. Assuming  $Z = 0.0246$  in the deeper layers and taking into account a slight He enrichment caused by depletion in Jupiter’s outer layers, we get  $Y = 0.2788$ . The assumed value of  $Z$  corresponds to abundances of  $\text{CH}_4$  and  $\text{NH}_3$ , relative to H, that are 4 times protosolar. Because of the much larger protosolar value of  $\text{H}_2\text{O}$  relative to H, a similar 4 times enhancement of this molecule leads to larger  $Z$  and hence interior densities, and the resulting models would be outside the acceptable range. We get  $Z = 0.0246$  if we take the enhancement of  $\text{H}_2\text{O}$  to be 2.4 times protosolar.

We insert this value in Equation (3) for the presumed jovian composition at layers with  $P > 2$  Mbar. Then, over a pressure range corresponding to the bulk of the jovian envelope,  $2 < P < 40$  Mbar, we find from Figure 6 and Figure 9 that  $\rho_0/\rho_{\text{He}} \approx 0.49$  and  $\rho_0/\rho_Z \approx 0.42$ , leading to  $\rho_0/\rho \approx 0.959$ .

As is obvious from these results, and has

long been known, the presence of metals in Jupiter only affects the barotrope  $\rho(P)$  at the level of a few percent. Thus modeling the abundance and distribution of metals in Jupiter by matching the planet’s gravity data necessarily requires very accurate (better than 1%) knowledge of  $\rho_0(P)$ .

## 5. Jupiter Models

### 5.1. Spheroid Parameters and Code Function

The version of the concentric maclaurin spheroid (CMS) code that we use is designed to automatically calculate a mass distribution with a total mass equal to Jupiter’s mass,  $M_J = 1.8986 \times 10^{30}$  g, and an equatorial radius  $a = 71492$  km. The latter is the observed equatorial radius of a layer at an average pressure of 1 bar, and the tabulated  $J_{2n}$  are normalized to this radius. We assume that Jupiter rotates as a solid body with period (Seidelmann et al. 2007)  $P_{\text{rot}} = 9^{\text{h}}55^{\text{m}}29.7^{\text{s}} = 2\pi/\omega$ . CMS theory is constructed to find a rotationally-distorted model for the dimensionless small parameter

$$q = \frac{\omega^2 a^3}{GM_J}, \quad (4)$$

which to lowest order in  $\omega^2$  is equivalent to  $m$ , see Equation (A2), but is more convenient as it can be directly computed from observed quantities.

Models are calculated with  $N + 1 = 511$  spheroids. Using the notation of Hubbard (2013), the dimensionless equatorial radii of the spheroids  $\lambda_i, i = 0, \dots, N$  are specified as follows. By definition  $\lambda_0 \equiv 1$  for the outermost spheroid (its equatorial radius  $\equiv a$ ). The innermost spheroid surface is placed at  $\lambda_N = 0.15$  (i.e., the core’s equa-

torial radius =  $0.15 a$ ). The choice of core radius is somewhat arbitrary: the external zonal harmonic coefficients are sensitive to the total core mass but insensitive to its density. Models have 170 spheroids equally spaced in  $\lambda$  in the range  $0.15 \leq \lambda \leq 0.5$  and another 339 spheroids in the range  $0.5 \leq \lambda \leq 1 - \delta\lambda/2$ . (where in this region the spacing  $\delta\lambda = 0.001477$ , or 105.6 km). The outermost spheroid ( $\lambda_0$ ) has zero density and is spaced  $\delta\lambda/2$  (or 53 km) above the next spheroid ( $\lambda_1$ ).

We verified that zonal gravitational harmonic results were unaffected by the details of the spheroid spacing, by carrying out subsidiary calculations with spheroids equally spaced from core to surface. As shown in Figure 13 for a typical Jupiter interior model, spheroids interior to  $\lambda \approx 0.5$  make no significant contribution to the  $J_n$ . Therefore we chose a closer spacing of spheroids exterior to  $\lambda = 0.5$ , to improve accuracy.

As outlined in Hubbard (2013), two nested iterations are required to obtain a converged rotationally-distorted model fitted to a given barotrope  $P(\rho)$ . Before the iterations begin, a provisional density distribution is specified, with each  $i^{\text{th}}$  spheroid having a constant density  $\rho_i$ . For the specified  $q$ , the shape and total potential of each  $i^{\text{th}}$  spheroid is then iteratively calculated until relative changes between iterations fall below a specified tolerance, usually  $\sim 10^{-13}$ . Typically, this requires  $\sim 30$  iterations. After satisfactory convergence, the total mass of the configuration  $M_{\text{conf}}$  is obtained by summing over all spheroids.

An outer iteration loop (typically  $\sim 50$  iterations) is performed to converge the

model to the specified barotrope  $P(\rho)$ . As described by Hubbard (2013), using the  $\rho_i$  and equipotential shapes from the converged inner loop, the average pressure  $P_i$  between the upper and lower surface of each spheroid is calculated. Then using the  $P_i$ , the barotrope relation is solved for each spheroid to obtain new density values,  $\rho_i = \rho(P_i)$ . The core spheroid is not included in this procedure as it is assumed to be an incompressible high-density region. See Section 17 for details on the convergence of the iterations.

Define the renormalization constant  $\beta = M_J/M_{\text{conf}}$ . After the latest outer iteration, we renormalize all the  $\rho_i$  by multiplying each value (including the core) by the factor  $\beta$ . These new  $\rho_i$  are then passed to the inner iteration loop, where the spheroid shapes and corresponding external  $J_{2n}$  are computed, and then  $M_{\text{conf}}$  (which depends on the spheroid shapes) is computed. The resulting configuration is then passed back to the outer loop.

The final result of the two iteration loops is a model with converged  $J_{2n}$ , a mass and rescaled density of the incompressible core, and spheroids  $i = 0, \dots, 509$  fitted to the *scaled* prescribed barotrope  $P = P(\beta\rho)$ . The model conforms precisely to the prescribed values of  $q$ ,  $a$ , and  $M_J$ . The scaled barotrope  $P = P(\beta\rho)$  corresponding to this model is convenient for comparing with barotropes for various values of  $Y$  and  $Z$ , e.g. of the form of Equation (3), in which the initial DFT-MD simulations for  $\rho_0(P)$  are rescaled by a (roughly constant) factor to account for new values of  $Y$  and  $Z$ . Values of  $\beta$  for each model are used to obtain results for the model's metals content  $Z$ , as entered

in Table 1.

Introduction of the renormalization constant  $\beta$  provides a convenient method for efficiently exploring the parameter space of jovian models, because, as discussed in Section 4, to first approximation the density  $\rho$  of a perturbed mixture of H, He, and metals is related to the reference mixture by the divisor  $\rho_0/\rho$  which is nearly constant over a broad range of pressures. Thus if  $\beta < 1$ , the overall metals content of the model is reduced with respect to the assumed starting barotrope, and *vice versa*.

## 5.2. Parameters of Barotrope and Core

For the reader’s assistance, Table 3 briefly defines a number of relevant parameters.

As discussed by Militzer et al. (2008), it is difficult to fit the pre-*Juno* values of Jupiter’s  $J_{2n}$ , especially  $J_4$ , with a constant-entropy, constant-composition barotrope and uniform rotation. Although the H-He DFT-MD equation of state has been updated since 2008, see Militzer & Hubbard (2013) and Militzer (2013), the difficulty remains. For comparison purposes, we include at the end of Table 1 two interior models (denoted as SC) that we computed using the same CMS procedure as the other models, but with the older equation of state of Saumon et al. (1995). These SC models are able to match the pre-*Juno*  $J_2$  and  $J_4$  with vanishingly-small cores and tens of Earth masses of metals in the envelope (see Table 1). Why are our DFT-MD models so different? Although central temperatures for DFT-MD and SC models are similar (see Table 1), it turns out that mid-envelope tempera-

tures for adiabatic DFT-MD models are considerably cooler. This behavior is a consequence of the depression of the adiabatic temperature gradient associated with hydrogen metallization, as discussed by Militzer & Hubbard (2013) and Militzer (2013). Such behavior is not exhibited by the SC EOS and may not be incorporated in the other recent Jupiter models. Cooler temperatures, as well as revisions to the pressure-density relation, result in somewhat higher mass densities in the middle envelope, with respect to the other models. It is this effect, in our models, that is primarily responsible for considerably reduced envelope metallicity, larger core mass, and increased  $|J_4|$ .

In 2008 we attempted to reduce the absolute value of  $J_4$  by hypothesizing a subtating layer below Jupiter’s observable atmosphere, but this assumption is not supported by any realistic circulation model. It is possible to obtain a model which fits the pre-*Juno* value of  $J_4$  by instead introducing a chemical change and corresponding extra density increase at layers around  $P \sim 1$  Mbar, but such models are not grounded in any fundamental calculations of the thermodynamics of dense hydrogen plus impurities, and are inconsistent with reasonable barotropes. In this paper we take a different approach. We use the Morales et al. (2013) prediction for the pressure-temperature conditions of H/He immiscibility. Then we assume helium rain also introduces a composition change. As discussed in Section 3, for  $P < 1$  Mbar, we have  $\rho_0/\rho = 0.995$ , while for  $P > 2.7$  Mbar, if one has four times solar (primordial) abundances of  $\text{CH}_4$ ,  $\text{NH}_3$ , and  $\sim 2.4$  times  $\text{H}_2\text{O}$ , and no other met-

als, as the composition at depth, one would have  $\rho_0/\rho = 0.959$ . These numbers suggest an expected extra  $\sim 4\%$  density change resulting from the presence of a phase-separation region and an increase of metallicity and helium to approximately protosolar values at deeper layers. As we discuss in more detail below, we need a much larger extra density change ( $\sim 8\%$ ) to obtain a DFT-MD model with  $|J_4|$  reduced enough to agree with the pre-*Juno* value.

To treat the expected extra density change, in the pressure range between 1 and 2 Mbar we interpolate linearly in  $\log P$  and  $\log \rho$  between the low-pressure barotrope with  $\rho = \rho_0(P)/0.995$  and the high-pressure barotrope with  $\rho = \rho_0(P)/0.959$ , noting that  $\rho_0(P)$  at  $P > 2.7$  Mbar lies on a higher-entropy adiabat than the atmospheric adiabat. Results for gravitational harmonic coefficients of models are insensitive to the thickness of this narrow interpolation region. A CMS boundary could of course be placed at a discrete location to exactly treat an actual density discontinuity, but the resulting change to the gravitational harmonic coefficients would be negligible.

The models presented in this paper are intended to correspond closely to the theoretical behavior of hydrogen-helium mixtures and to properties of the outer jovian layers as constrained by the Galileo Probe.

The CMS method generates models that exactly fit the total jovian mass and 1-bar equatorial radius. We adjust the density (and thus the mass) of the schematic central core of all models to obtain a match to the pre-*Juno* observed value of  $J_2$  given in Table 1, in the expectation that a more precise post-*Juno* value will not differ sig-

nificantly from this number. The other parameter beside the core mass that is poorly constrained is the entropy of the deep adiabat, which we vary from the Galileo Probe value  $S = 7.08$  through the value that oscillates the immiscibility boundary,  $S = 7.20$ , on up to (as an extreme case)  $S = 7.24$ . With increasing  $S$ , the thermal contribution to the deep pressure increases, yielding lower density for a given pressure, thus accommodating a slight increase in metallicity  $Z$ . As we see from Table 1, the predicted higher-order gravitational harmonic coefficients vary from one model to the next at the level of  $\sim 10^{-5}$  for  $J_4$  (readily measurable by *Juno*), to  $\sim 10^{-6}$  for  $J_6$ , to  $\sim 10^{-8}$  for  $J_8$ . The  $J_{10}$  values appear to have less value for discriminating interior structure, but their near-constancy at a total level of  $\sim 10^{-7}$  may be useful as a reference for discerning the signature of nonhydrostatic effects at a similar level, such as deep interior dynamics (Kaspi et al. 2010).

By increasing the density by an additional amount in the vicinity of the He-immiscibility zone, it is possible to obtain a match to Jupiter’s pre-*Juno*  $J_2$  and  $J_4$  with a suitable model. But, as noted by Militzer et al. (2008), one does not have free rein in this process because Jupiter’s barotrope must correspond to a physically-plausible composition. Because the DFT-MD barotrope is generally denser than the corresponding barotrope that one would compute using the theory of Saumon et al. (1995), in our DFT-MD models very little enhancement of metals can be tolerated in Jupiter’s envelope.

Most of our models are calculated using (for  $P < 1$  Mbar) the barotrope  $\rho = \rho_0(P, S = 7.08)/0.995$ , corresponding to

the Galileo Probe  $T(P)$  and abundances, and the barotrope  $\rho = \rho_0(P, S)/0.959$  for  $P > 2.7$  Mbar, corresponding to an adiabat with entropy  $S > 7.08$ , (enhanced) protosolar helium abundance  $Y = 0.28$ , and  $Z = 0.025$ , corresponding to Galileo-Probe enhancement of methane and ammonia and a lesser enhancement of water, but no presence of denser species such as magnesium-silicates. During the CMS calculations we linearly interpolate in  $\log \rho$  vs.  $\log P$  across the immiscibility region between 1 and 2.7 Mbar. All models in Table 1 labeled DFT-MD  $S$  (with no parenthesis) have the indicated compositions in the molecular and metallic regions respectively. As the deep  $S$  increases, such models show a modest increase in metallicity in the hydrogen-helium envelope exterior to the dense core, as characterized by the parameter  $M_Z$ , the total mass of metals in Earth masses.

Model DFT-MD 7.13 has  $\beta = 1.0000$ , meaning that the input barotrope yields a match to the total planetary mass without rescaling the densities. A characteristic of DFT-MD 7.13 warrants discussion. This model has Galileo Probe abundances of  $\text{CH}_4$ ,  $\text{NH}_3$ , and  $\text{H}_2\text{O}$  *throughout* the molecular layer, and  $4\times$  solar abundances of  $\text{CH}_4$ , and  $\text{NH}_3$  in the metallic layer. The metallic layer has  $2.4\times$  solar  $\text{H}_2\text{O}$ , more than in the molecular layer; a full  $4\times$  solar  $\text{H}_2\text{O}$  enhancement would yield total densities which are too large to fit the total mass of Jupiter. As discussed in Section 4, the assumed composition and temperature profile results in a reasonable  $\rho(P)$  relation, which results in a reasonable planetary model. However, acceptable  $\rho(P)$  relations only limit the possible range of temperature profiles and metallicities but

do not uniquely constrain them.

As alternatives, we investigated two variants of our preferred model, in which we imposed equal metallicities in the molecular and metallic layers. Model DFT-MD 7.13 (low- $Z$ ) has artificially low  $Z = 0.004$  in both layers (although He abundance does increase from the Galileo probe value to the protosolar value). This unrealistic model has the largest  $|J_4|$  and core mass of the suite. At the opposite extreme, Model 7.24 (equal- $Z$ ) has the same metallicity  $Z = 0.027$  in both layers, and also has a relatively large  $|J_4|$ .

All models shown in Table 1 have core mass adjusted to give agreement to seven significant figures with the observed value  $J_2 = 14696.43 \times 10^{-6}$ . Two of the models, DFT-MD 7.15(J4) and SC 7.15(J4), include an additional density (and metallicity) increase across the immiscibility region between 1 and 2 Mbar, adjusted to yield agreement with the pre-*Juno* observed values of  $J_2$  and  $J_4 = -587.14 \times 10^{-6}$ . We note that uncertainties in observed values in Table 1 are formal error bars; none of our models would be ruled out by these pre-*Juno* measurements if the true error bars are  $\sim 5$  times larger. All of our models are close to the pre-*Juno* observed value of  $J_6$ , but the agreement may be fortuitous.

### 5.3. Comparison of Barotropes with Models

Figure 10 shows a plot of polar and equatorial density profiles for our preferred model DFT-MD 7.13.

Figure 11 plots the density vs. pressure profile for preferred model DFT-MD 7.13 (grey staircase), along with the input barotrope. Figure 12 is a close-up

of the high-pressure region of Figure 11. The weighting functions for contributions to the external zonal harmonic coefficients, for the preferred model, are shown in Figure 13.

Model DFT-MD 7.15(J4) reduces  $|J_4|$  to the observed value by decreasing the barotrope’s density at low pressures, and increasing the density at high pressures. However, densities in the outer region at pressures below 1 Mbar then correspond to unphysical negative metallicity. The entry for this model in Table 1 shows a total metals content  $M_Z = 14.3 M_E$  exterior to the dense core; this value is the sum of  $14.9 M_E$  in the H-He envelope at pressures greater than  $\sim 1$  Mbar, and (unphysical)  $-0.6 M_E$  at lower pressures. We are unable to find a consistent DFT-MD Jupiter model that matches the observed  $J_2$  and  $J_4$  values in Table 1.

## 6. Moment of Inertia

Jupiter’s normalized moment of inertia  $\text{NMoI} = C/Ma^2$  (where  $C$  is the moment of inertia about the rotation axis) is in principle separately measurable from the  $J_{2n}$ , and is a separate constraint on interior structure. Helled et al. (2011) investigate models with fixed values of  $J_2$  and  $J_4$  and conclude that a range of NMoI values between 0.2629 and 0.2645 can be found. Nettelmann et al. (2012) calculate a moment of inertia but normalize it to the *mean* radius of the 1-bar equipotential surface, a model-dependent quantity with a precision limited to third order in their perturbative theory of figures. However, their result is in reasonable agreement with values that we calculate below. Since the nonperturbative approach of our present

investigation virtually eliminates any uncertainty in the theoretical calculation of the  $J_{2n}$ , here we explore the subject further as a guide to measurement requirements for the *Juno* spacecraft.

Once a converged interior model is obtained, the NMoI is given exactly by the expression

$$\frac{C}{Ma^2} = \frac{2 \sum_{j=0}^{N-1} \delta\rho_j \int_0^1 d\mu \xi_j(\mu)^5}{5 \sum_{j=0}^{N-1} \delta\rho_j \int_0^1 d\mu \xi_j(\mu)^3} + \frac{2}{3} J_2, \quad (5)$$

in the notation of Hubbard (2013).

Although Equation (5) resembles the Radau-Darwin relation in that it seemingly relates the NMoI to  $J_2$ , it actually has no relationship because Equation (5) shows that for a fixed  $J_2$ , an infinity of different CMS density distributions could enter into the first term. On the other hand, since each of those CMS density distributions is required to yield the fixed  $J_2$ , the range of variation of NMoI is in actuality quite restricted. To illustrate the point, in Figure 14 we show the cumulative value of the NMoI as a function of the CMS radius  $\lambda$ , for preferred model DFT-MD 7.13. The cumulative value of  $C/Ma^2$  is obtained by partially summing the expression in Equation (5) from the central CMS ( $j = N - 1$ ) out to a CMS with dimensionless equatorial radius  $\lambda$ .

To illustrate how details of interior structure affect the total NMoI, Figure 15 shows the *difference* of the cumulative values of  $C/Ma^2$ , for the preferred model minus model SC 7.15.

To truly discriminate between models with different barotropes, it will be necessary to measure the NMoI to about five significant figures, posing a difficult challenge

to *Juno* or other future investigations. Figure 16 illustrates the point.

We should point out that a measurement of Jupiter’s NMoI would actually be obtained from a measurement of the planet’s spin angular momentum,  $J = C\omega$ . Thus if Jupiter were to rotate differentially on cylinders with significant mass involved in the various rotation zones, the tightly constrained values of NMoI that we find here might be broadened to some extent. It remains to be determined whether measurement of NMoI will prove to be more of a constraint on the possibility of deep differential rotation, or on the range of possible interior barotropes.

## 7. Discussion and Conclusions

The combination of the DFT-MD equation of state and observed  $J_{2n}$  already strongly limit the parameter space of acceptable pre-*Juno* models.

Our study has the following new features: (a) We eliminate arbitrary density enhancements to fit the gravity field; instead we utilize the H-He immiscibility phase boundary computed by Morales et al. (2013) to bound the location and magnitude of a helium-related compositional change; (b) Our models incorporate the latest version of the DFT-MD equation of state, replacing the widely-used SC EOS theory (Saumon et al. 1995); (c) We utilize CMS theory for the first time to calculate high-order zonal harmonic coefficients for realistic Jupiter models.

It is important to note that for fixed  $J_2$ , the computed value of  $|J_4|$  is sensitive to the density in the region of Jupiter’s metallic-hydrogen envelope where He im-

miscibility is predicted. One may force an agreement with the pre-*Juno* value of  $J_4$  given in Table 1 by imposing a density enhancement across the interpolation region which is much larger than the  $\sim 4\%$  implied by an increase in He to the primordial value above  $P > 2.7$  Mbar. However, when this is done, conservation of mass leads to a model with (formally) negative metallicity in the low-pressure outer envelope.

The new DFT-MD equation of state generally yields a very limited suite of interior models of relatively low metallicity. These models could be falsified by forthcoming *Juno* gravity data.

In Jupiter model DFT-MD 7.13, about 0.83 of the total mass is between the He-immiscibility region near 1 Mbar pressure and the core-mantle boundary. So if  $Z \sim 0.032$  in this region, the mass of metals outside the core would comprise  $\sim 10M_E$ , to be added to a core mass  $\sim 12M_E$ , for a total Jupiter metallicity  $Z_{\text{global}} \sim 0.07$ . As shown in Table 1, most of the other DFT-MD models have similar total metallicities. In contrast, our models based on the SC EOS (last two lines in Table 1) have total metallicities that are about 60% higher, in qualitative agreement with earlier results obtained by Guillot et al. (1997) and Guillot (1999) that were also derived using the SC equation of state. The latter studies included the possibility that Jupiter’s core mass might be zero, and our independent SC models also show very small core masses.

The inferred large core masses of our DFT-MD models are consistent with a core-nucleated scenario for the formation of Jupiter (D’Angelo et al. 2014). The

overall metallicity of Jupiter implied by most of our models is roughly three times protosolar, implying that about two-thirds of the volatile protosolar nebular complement to the  $\sim 12M_E$  refractory core was not incorporated in primordial Jupiter.

In summary, we are able to derive Jupiter interior models that match measured values of  $J_2$ , and sometimes  $J_4$ , and  $J_6$ , and are consistent with predictions from published *ab initio* simulations of hydrogen and helium, and additional results for different planetary ices,  $H_2O$ ,  $CH_4$ , and  $NH_3$  that we report here. In our preferred model, the heavy element abundance in the metallic layer is equivalent to a three-fold solar concentration of all three ices. The preferred value for the concentration in the molecular layer is slightly less but consistent with the Galileo measurements.

Our preferred model has a massive core of 12 Earth masses which is very similar to our earlier model (Militzer et al. 2008). When one uses the semi-analytical equation of state (SC EOS) of Saumon et al. (1995) instead of our *ab initio* DFT-MD EOS, a much smaller core of 4 Earth masses is predicted for the same model assumptions. This illustrates how sensitively some model predictions depend on the details of hydrogen-helium EOS.

Our Jupiter model is preliminary and intended for use as a reference for comparison with experimental results from the *Juno* orbiter and other data sources. New data will tell us how well the model works.

This work has been supported by NASA and NSF.

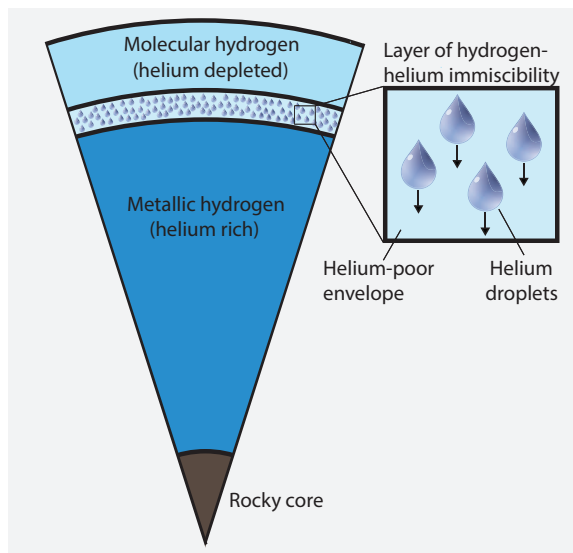


Fig. 2.— Diagram showing the location of the hydrogen-helium immiscibility layer in Jupiter.

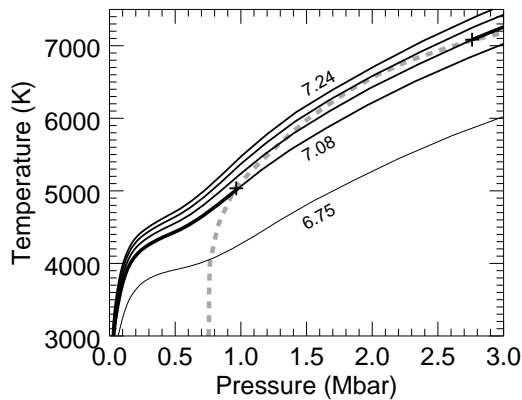


Fig. 3.— Temperature-pressure relations used in the models. DFT-MD adiabats are labeled with their entropy per electron  $S = 7.24$  (top) to  $6.75$  (bottom). The two middle (unlabeled) adiabats have  $S = 7.20$  and  $7.13$ . The preferred temperature-pressure relation of this paper is shown as a heavier curve following the Galileo Probe adiabat to the immiscibility boundary (Morales et al. 2013) shown with a dashed curve. At pressures higher than 2.7 Mbar we assume a higher-entropy adiabat with  $S = 7.13$  (heavier curve).

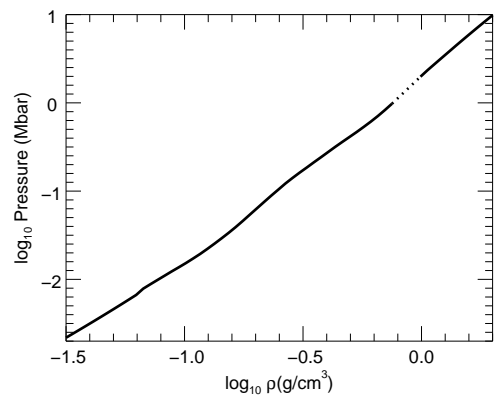


Fig. 4.— The initial approximation for the present-Jupiter barotrope; the abscissa is  $\rho_0(P)$ . The gap corresponds to the region between the two plus symbols in Figure 3. To the left of the gap the entropy is  $S = 7.08$ , while to the right  $S = 7.13$ . Both adiabats are for constant  $Y_0=0.245$ . Since we do not have DFT-MD simulation data at very low densities, we switch back to the SC model below  $0.0670 \text{ g cm}^{-3}$ , where a small (and unimportant) density discontinuity  $\sim 2\%$  can be seen.

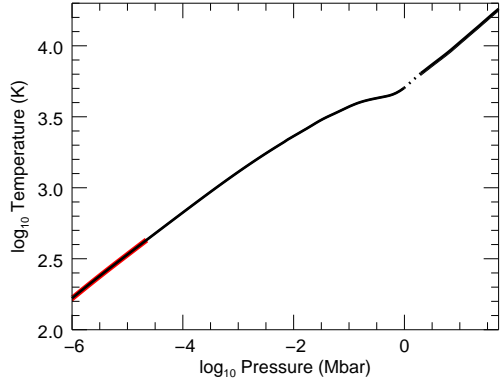


Fig. 5.— The  $T$  vs.  $P$  relation for the two adiabats shown in Figure 4. Thick curve up to  $P = 22$  bar shows Galileo Probe measurements. The  $S = 7.08$  adiabat's  $T$  vs.  $P$  relation matches Galileo Probe data.

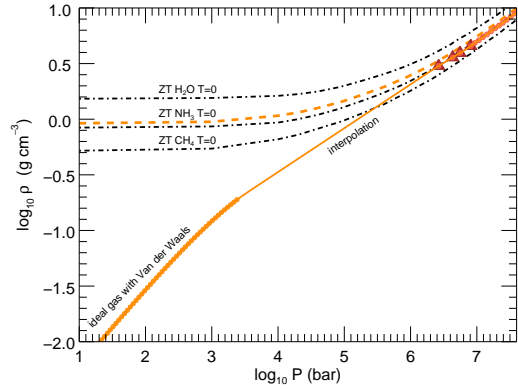


Fig. 7.— Procedure for determining the compression of a solar-proportions mixture of  $\text{CH}_4$ ,  $\text{NH}_3$ , and  $\text{H}_2\text{O}$  (the three most important jovian hydrides) along a jovian  $T(P)$  curve. This relation is used to determine  $\rho_Z(P)$ . Van der Waals corrections for the three hydrides are computed using data from Weast (1972).

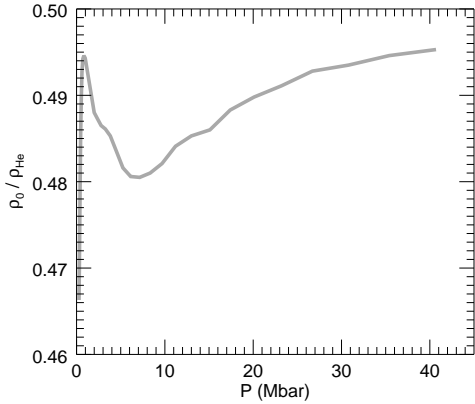


Fig. 6.— Results for  $\rho_0/\rho_{\text{He}}$ , evaluated along a Jupiter barotrope, to be inserted in Equation (3).

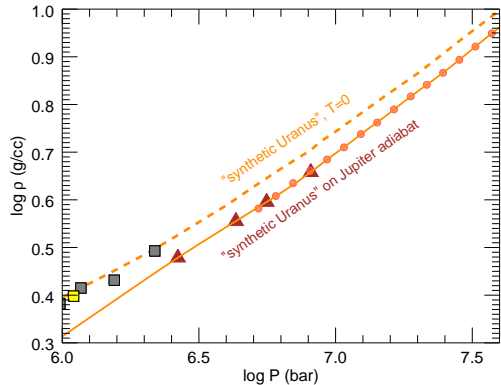


Fig. 8.— Expanded view of the high-pressure region of Figure 7. Brown triangles show results of our DFT-MD simulations for a solar-proportions mixture of  $\text{CH}_4$ ,  $\text{NH}_3$ , and  $\text{H}_2\text{O}$  at four points on the jovian  $T(P)$  curve. These results overlap with results for a simple Mie-Grüneisen thermal perturbation (with a Grüneisen  $\gamma = 1$ ) plus zero-temperature pressure, smaller red dots. Squares show double-shock compression points from Livermore gas gun experiments on “synthetic Uranus” carried out by Nellis et al. (1997). A temperature  $T = 4100 \pm 300$  K was measured for the data point at 1.1 Mbar, plotted as a yellow square. A separate DFT-MD simulation agrees with this data point to within the error bars, but is not used to calibrate our  $\rho_Z(P)$  curve.

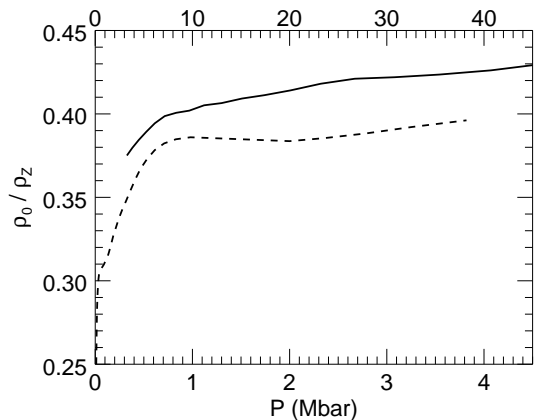


Fig. 9.— Results for  $\rho_0/\rho_Z$ , evaluated along a Jupiter barotrope. The dashed curve shows results for low pressures, spanning Jupiter’s “molecular” layer (corresponding to the lower pressure axis). The solid curve (corresponding to the upper pressure axis) shows results for pressures up to the core-mantle boundary and slightly different composition, spanning Jupiter’s “metallic” layer. These relations are inserted into Eq. 3; see Section 4 for details.

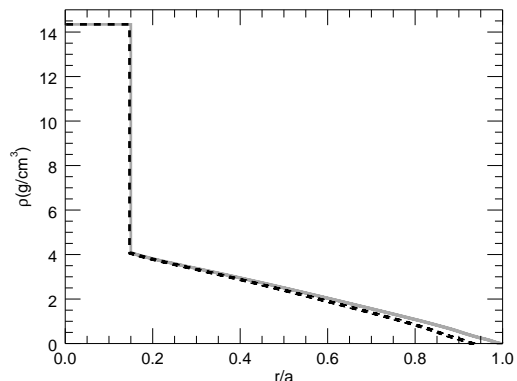


Fig. 10.— Equatorial (solid curve) and polar (dashed curve) density profiles.

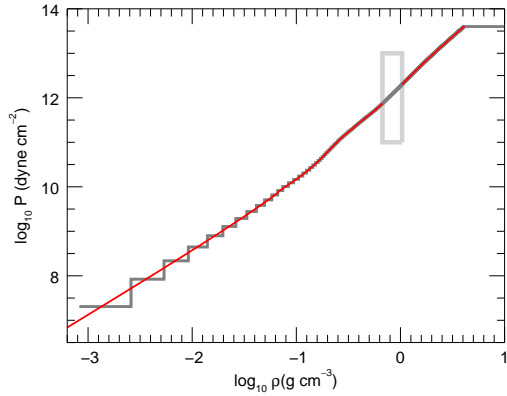


Fig. 11.— The grey staircase shows converged CMS model DFT-MD 7.13. The light grey rectangle shows the region where He immiscibility occurs and where the barotrope is interpolated to a higher-entropy barotrope at higher pressure. The red curve is the input barotrope for the assumed low-pressure and high-pressure compositions.

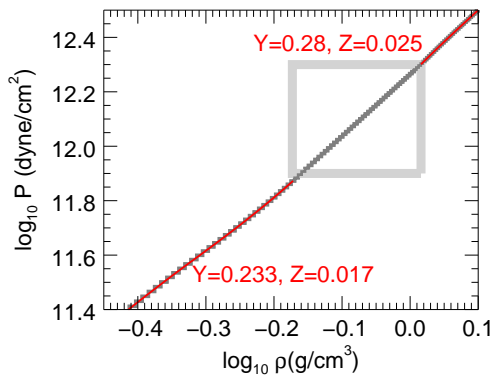


Fig. 12.— A close-up of the barotrope interpolation region for preferred CMS model DFT-MD 7.13. The red curve is the input barotrope for the assumed compositions.

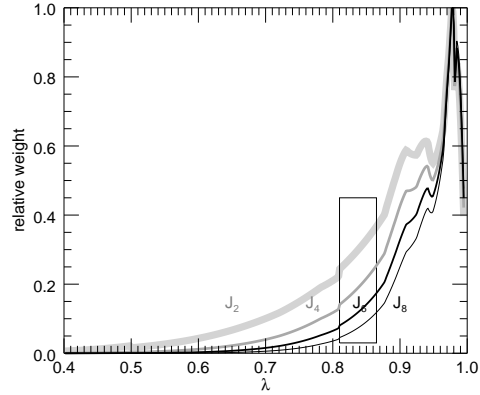


Fig. 13.— Relative contribution of spheroids to external gravitational zonal harmonic coefficients, for model DFT-MD 7.13.

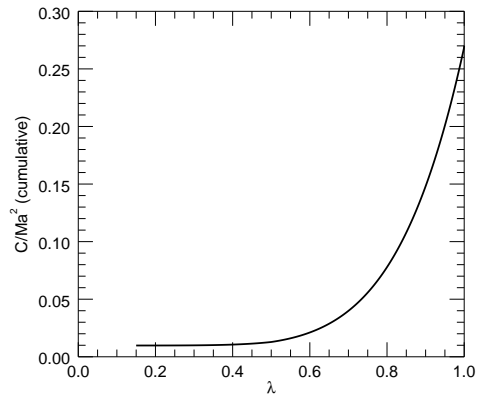


Fig. 14.— Cumulative value of  $C/Ma^2$  for the preferred Jupiter model. The final point at  $\lambda = 1$  is the total value,  $C/Ma^2 = 0.26389$ .

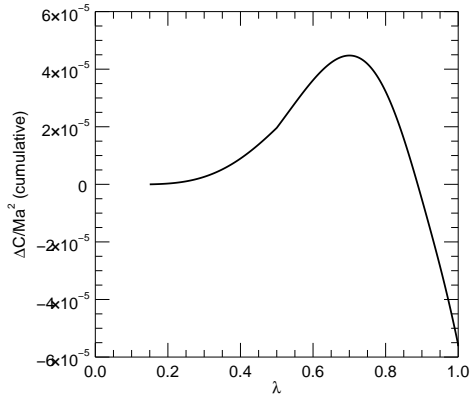


Fig. 15.— Difference in cumulative values of  $C/Ma^2$  for the preferred Jupiter model minus model with the SC equation of state.

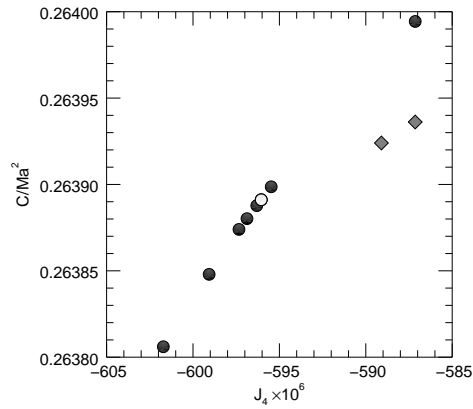


Fig. 16.— For the ten interior models of Table 1, all fixed to the observed  $J_2$ , we plot the NMoI vs.  $J_4$ . The open circle is the preferred model. The two diamonds to the right are the SC models.

## A. Definitions for theory of figures

The external potential of a liquid planet in hydrostatic equilibrium rotating at a uniform rate  $\omega$  is usually expanded on Legendre polynomials  $P_{2n}(\mu)$  as

$$V(r, \mu) = \frac{GM}{r} \left[ 1 - \sum_{n=1}^{\infty} \left(\frac{a}{r}\right)^{2n} J_{2n} P_{2n}(\mu) \right] \quad (\text{A1})$$

where  $G$  is the gravitational constant,  $M$  the planet's mass,  $a = 71492$  km is the normalizing radius,  $\mu$  is the cosine of the angle from the rotation axis, and  $r$  the radial distance from the center of mass. Pre-*Juno* values of Jupiter's zonal harmonic coefficients  $J_{2n}$  are given in the first line of Table 1, and are identical to values cited by Militzer et al. (2008).

It is expected that the *Juno* gravity experiment will improve the precision of the harmonic coefficients by at least two orders of magnitude and measure the coefficients to degree 10 and possibly beyond. Values of the  $J_{2n}$  provide integral constraints on the mass distribution within Jupiter, and can thus be used to constrain interior models. As discussed by Hubbard et al. (2013), the basic parameter that determines the magnitude of the  $J_{2n}$  is the dimensionless number  $m$  (to lowest order,  $m$  is the ratio of the magnitude of the rotational acceleration to gravitational acceleration, at the planet's equator),

$$m = \frac{3\omega^2}{4\pi G\bar{\rho}}, \quad (\text{A2})$$

where  $\bar{\rho}$  is Jupiter's mean density. Zharkov & Trubitsyn (1978) show that one may write

$$J_{2n} = m^n \sum_{t=0}^{\infty} \Lambda_{2n}^{(t)} m^t, \quad (\text{A3})$$

where the dimensionless response coefficients,  $\Lambda_{2n}^{(t)}$ , can be obtained from the solution of a hierarchy of nonlinear perturbation equations. These response coefficients in turn depend on the equation of state relating the pressure  $P$  to the mass density  $\rho$  at each point within the planet. Provided that a barotropic relation  $P(\rho)$  exists and that the planet is in hydrostatic equilibrium, the perturbative potential-theory approach of Zharkov & Trubitsyn (1978) can be used. However,  $m \approx 0.08$  for Jupiter and  $m \approx 0.14$  for Saturn, and the dimensionless coefficients  $\Lambda_{2n}^{(t)}$  do not decline rapidly with  $n$  and  $t$ . Replacing the infinite sum in Equation (A3) with a finite sum up to, say  $t \approx 9$  might suffice to determine the measurable  $J_{2n}$  to better than *Juno* precision, but would entail evaluation of lengthy analytic expressions. Instead, in this paper we use the more straightforward non-perturbative concentric maclaurin spheroid (CMS) theory of figures of Hubbard (2013).

## B. Numerical precision of CMS calculations

Figure 17 shows the improvement in the  $J_{2n}$  values for a typical model over 50 steps in the outer iteration loop. After 50 iterations, the change in  $J_{12}$  and higher degrees has fallen

below the computer's floating point precision. The change in  $J_2$  after 50 steps is at the level of  $10^{-11}$ , much smaller than the precision with which it can be measured.

Figure 18 shows the relative error in the CMS calculation of the gravitational potential on the level surfaces of a converged model using the audit-point method described in Hubbard et al. (2013).

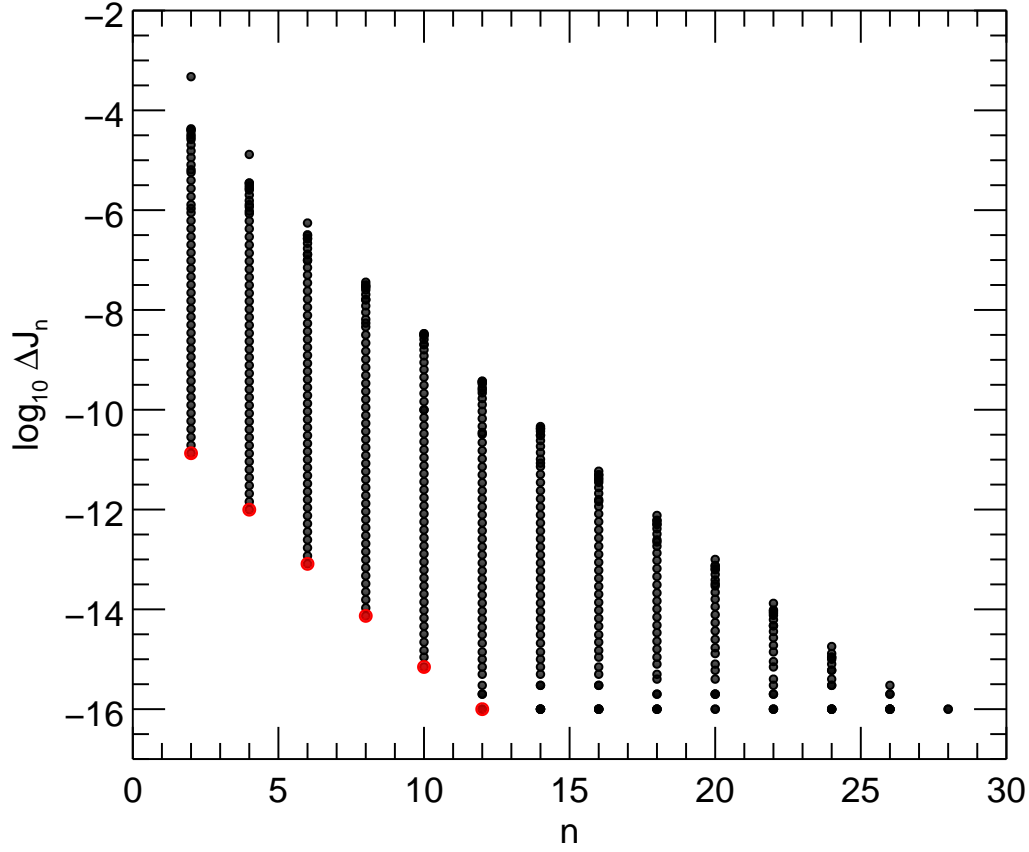


Fig. 17.— Improvement in the value of external zonal gravitational harmonic coefficients over 50 steps in the outer iteration loop. Here  $\Delta J_n$  is the absolute value of the change of  $J_n$  from the previous iteration; the lowest points are the values of the changes after the last iteration.

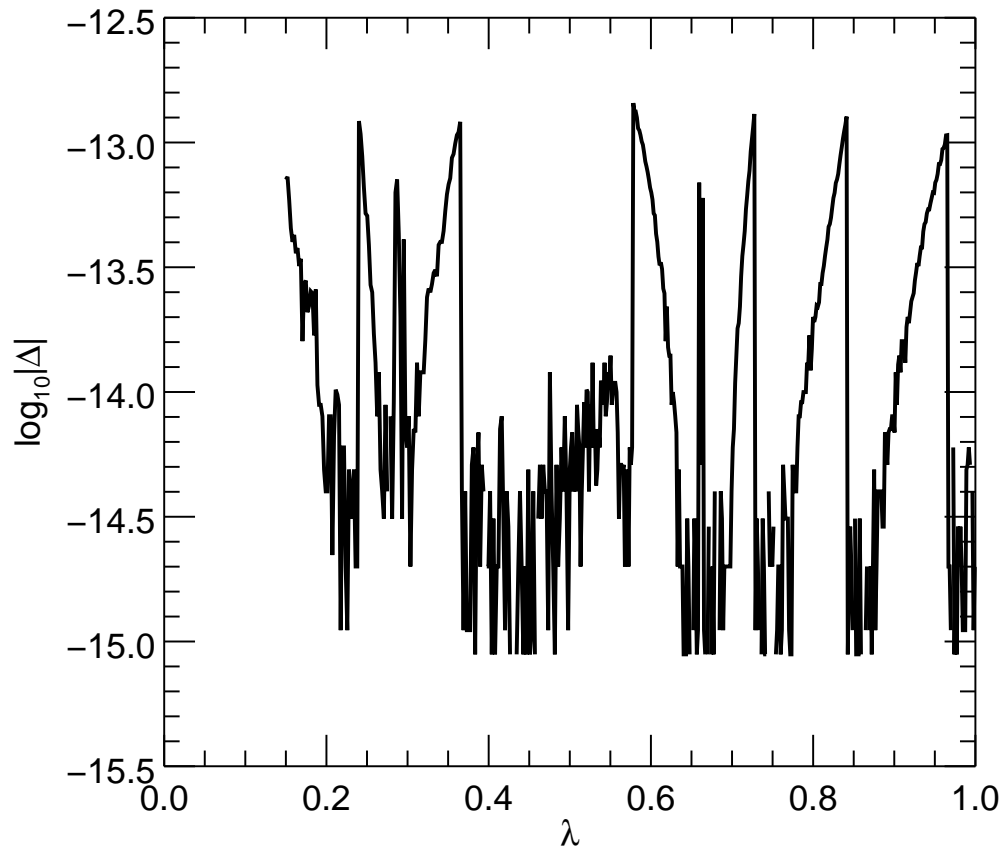


Fig. 18.— Here  $\Delta$  is the difference between the polar potential and the equatorial potential (in units of  $GM/a$ ), evaluated after 30 inner-loop iterations within 50 outer-loop iterations.

## REFERENCES

- Becker, A., Lorenzen, W., Fortney, J., Nettelmann, N., Schöttler, M., & Redmer, R. 2014, *Astrophys. J. Supp.*, 215, 21
- Blöchl, P. E. 1994, *Phys. Rev. B*, 50, 17953
- D'Angelo, G., Weidenschilling, S. J., Lissauer, J. J., & Bodenheimer, P. 2014, *Icarus*, 241, 298
- Fortney, J. J., & Hubbard, W. B. 2004, *Astrophys. J.*, 608, 1039
- Gonzalez-Cataldo, F., Wilson, H. F., & Militzer, B. 2014, *Astrophys. J.*, 787, 79
- Guillot, T. 1999, *Planetary and Space Science*, 47, 1183
- Guillot, T., Gautier, D., & Hubbard, W. B. 1997, *Icarus*, 130, 534
- Helled, R., Anderson, J., Schubert, G., & Stevenson, D. 2011, *Icarus*, 216, 440
- Hubbard, W. B. 2013, *Astrophys. J.*, 768, 43
- Hubbard, W. B., Schubert, G., Kong, D., & Zhang, K. 2013, *Icarus*, 242, 138
- Kaspi, Y., Hubbard, W. B., Showman, A. P., & Flierl, G. R. 2010, *Geophys. Res. Lett.*, 37, L01204
- Knudson, M. D., Desjarlais, M. P., Lemke, R. W., Mattsson, T. R., French, M., Nettelmann, N., & Redmer, R. 2012, *Phys. Rev. Lett.*, 108, 091102
- Kresse, G., & Furthmüller, J. 1996, *Phys. Rev. B*, 54, 11169
- Lindal, G. F., Sweetnam, D. N., & Eshleman, V. R. 1985, *Astron. J.*, 90, 1136
- Lodders, K. 2003, *Astrophys. J.*, 591, 1220
- Mahaffy, P. R., Niemann, H. B., Alpert, A., Atreya, S. K., Demick, J., Donahue, T. M., Harpold, D. N., & Owen, T. C. 2000, *J. Geophys. Res.*, 105, 15061
- Militzer, B. 2013, *Phys. Rev. B*, 87, 014202
- Militzer, B., & Hubbard, W. B. 2013, *Astrophys. J.*, 774, 148
- Militzer, B., Hubbard, W. H., Vorberger, J., Tamblyn, I., & Bonev, S. A. 2008, *Astrophys. J. Lett.*, 688, L45
- Morales, M. A., Hamel, S., Caspersen, K., & Schweigler, D. M. E. 2013, *Phys. Rev. B*, 87, 174105
- Nellis, W., Holmes, N., Mitchell, A., Hamilton, D., & Nicol, M. 1997, *J. Chem. Phys.*, 107, 9096
- Nettelmann, N., Becker, A., Holst, B., & Redmer, R. 2012, *Astrophys. J.*, 750, 52
- Nettelmann, N., Fortney, J., Moore, K., & Mankovich, C. 2015, *MNRAS*, 447, 3422
- Perdew, J. P., Burke, K., & Ernzerhof, M. 1996, *Phys. Rev. Lett.*, 77, 3865
- Saumon, D., Chabrier, G., & Horn, H. M. V. 1995, *Astrophys. J. Suppl.*, 99, 713
- Seidelmann, P. K., et al. 2007, *Celestial Mechanics and Dynamical Astronomy*, 98, 155
- Seiff, A., et al. 1998, *J. Geophys. Res.*, 103, 22857
- Stevenson, D., & Salpeter, E. 1977a, *Astrophys. J. Suppl. Ser.*, 35, 221

- . 1977b, *Astrophys. J. Suppl.*, 35, 239
- von Zahn, U., Hunten, D. M., & Lehman, G. 1998, *J. Geophys. Res.*, 103, 22815
- Vorberger, J., Tamblyn, I., Militzer, B., & Bonev, S. 2007, *Phys. Rev. B*, 75, 024206
- Wahl, S. M., Wilson, H. F., & Militzer, B. 2013, *Astrophys. J.*, 773, 95
- Weast, R. C. 1972, *Handbook of Chemistry and Physics* 53rd Ed. (Chemical Rubber Co.), D-166
- Wilson, H. F., & Militzer, B. 2010, *Phys. Rev. Lett.*, 104, 121101
- . 2012a, *Astrophys. J.*, 745, 54
- . 2012b, *Phys. Rev. Lett.*, 108, 111101
- Wong, M., Mahaffy, P. R., Atreya, S. K., Niemann, H. B., & Owen, T. C. 2004, *Icarus*, 171, 153
- Zharkov, V. N., & Trubitsyn, V. P. 1978, *Physics of Planetary Interiors* (Pachart, Tucson)

TABLE 1  
 JUPITER ZONAL HARMONIC COEFFICIENTS<sup>a</sup> AND MODEL VALUES (PREFERRED MODEL  
 IN BOLDFACE<sup>b</sup>)

(all $J_n \times 10^6$ )	$J_4$	$J_6$	$J_8$	$J_{10}$	$C/Ma^2$	$M_{\text{core}}$ ( $M_E$ )	$M_{Z,\text{molec.}}$ ( $M_E$ )	$M_{Z,\text{metal.}}$ ( $M_E$ )	$Z_{\text{global}}$	$T_{\text{CMB}}$ (K)
pre-Juno observed (JUP230) <sup>a</sup>	-587.14 $\pm 1.68$	34.25 $\pm 5.22$	...	...	...	...	...	...		
DFT-MD 7.24	-597.34	35.30	-2.561	0.212	0.26387	12.5	0.9	10.3	0.07	17600
DFT-MD 7.24 (equal- $Z$ )	-599.07	35.48	-2.579	0.214	0.26385	13.1	1.1	7.5	0.07	17650
DFT-MD 7.20	-596.88	35.24	-2.556	0.211	0.26388	12.3	0.8	9.9	0.07	17260
DFT-MD 7.15	-596.31	35.18	-2.549	0.211	0.26389	12.2	0.7	9.2	0.07	16860
DFT-MD 7.15 ( $J_4$ )	-587.14	34.17	-2.450	0.201	0.26399	9.7	-0.6	14.9	0.08	16770
<b>DFT-MD 7.13</b>	<b>-596.05</b>	<b>35.15</b>	<b>-2.546</b>	<b>0.210</b>	<b>0.26389</b>	<b>12.2</b>	<b>0.7</b>	<b>8.9</b>	<b>0.07</b>	<b>16670</b>
DFT-MD 7.13 (low- $Z$ )	-601.72	35.77	-2.608	0.217	0.26381	14.0	0.2	1.1	0.05	16820
DFT-MD 7.08	-595.47	35.08	-2.539	0.210	0.26390	12.0	0.6	8.3	0.07	16220
SC 7.15	-589.10	34.86	-2.556	0.214	0.26392	4.8	3.5	28.2	0.11	18020
SC 7.15 ( $J_4$ )	-587.14	34.65	-2.534	0.212	0.26394	4.3	3.2	29.3	0.12	17310

<sup>a</sup>Observed values are from R. A. Jacobson (2003), JUP230 orbit solution, with  $J_2 = (14696.43 \pm 0.21) \times 10^{-6}$ . All theoretical models match  $J_2 = 14696.43 \times 10^{-6}$  to seven significant figures.

<sup>b</sup> $\sim 0.83$  of the total mass is in the metallic layer, i.e. between  $\sim 2$  Mbar and the CMB at  $\sim 40$  Mbar.

TABLE 2

COMPARISON OF SHOCK WAVE MEASUREMENTS BY NELLIS ET AL. (1997) AND OUR *ab initio* SIMULATIONS THAT USED TWO COMPOSITIONS (A) H:O:C:N=87:25:13:4 AND (B) H:O:C:N=99:21:12:3.

Method	H:O	C:O	N:O	$\rho$ (g cm <sup>-3</sup> )	$T$ (K)	$P$ (GPa)
Experiment	3.54	0.529	0.162	$2.044 \pm 0.005$	$3220 \pm 200$	$49.9 \pm 0.5$
Simulation <sup>(a)</sup>	3.48	0.520	0.160	2.044	3220	$52.17 \pm 0.17$
Simulation <sup>(a)</sup>	3.48	0.520	0.160	2.039	3020	$50.17 \pm 0.30$
Experiment	3.54	0.529	0.162	$2.45 \pm 0.13$	$4100 \pm 300$	$110 \pm 4$
Simulation <sup>(a)</sup>	3.48	0.520	0.160	2.450	4100	$96.34 \pm 0.42$
Simulation <sup>(a)</sup>	3.48	0.520	0.160	2.580	4400	$114.47 \pm 0.35$
Simulation <sup>(b)</sup>	4.71	0.571	0.143	2.353	4100	$117.90 \pm 0.32$
Simulation <sup>(b)</sup>	4.71	0.571	0.143	2.262	4100	$105.37 \pm 0.25$
Simulation <sup>(b)</sup>	4.71	0.571	0.143	3.011	7000	$264.92 \pm 0.48$
Simulation <sup>(b)</sup>	4.71	0.571	0.143	3.592	8000	$431.78 \pm 0.34$
Simulation <sup>(b)</sup>	4.71	0.571	0.143	3.940	9000	$559.32 \pm 0.42$
Simulation <sup>(b)</sup>	4.71	0.571	0.143	4.550	10000	$811.62 \pm 0.56$

TABLE 3  
DEFINITIONS OF SOME PARAMETERS USED IN THIS PAPER

Parameter(s)	Definition
$X_0, Y_0$	mass fractions of H and He in DFT-MD simulations; see Equation (1)
$\rho_0$	mass density of H-He mixture in DFT-MD simulations, for given $P$ and $T$
$X, Y, Z$	perturbed mass fractions of H, He, and metals; see Equation (2)
$Z_{\text{global}}$	total mass fraction of “metals” in Jupiter (including dense core)
$\rho_0/\rho$	ratio of mass density for reference barotrope, Equation (1), to mass density with perturbed $X, Y, Z$
$\rho_0/\rho_{He}$	ratio of mass density for reference barotrope, Equation (1), to mass density of pure He at same $P$ and $T$
$\rho_0/\rho_Z$	ratio of mass density for reference barotrope, Equation (1), to mass density of a pure “metals” mixture at same $P$ and $T$
$M_E$	mass of the Earth
$M_{Z,\text{molec.}}$	total mass of $\text{CH}_4 + \text{NH}_3 + \text{H}_2\text{O}$ in Jupiter’s molecular layer; see Table 1
$M_{Z,\text{metal.}}$	total mass of $\text{CH}_4 + \text{NH}_3 + \text{H}_2\text{O}$ in Jupiter’s metallic layer; see Table 1
$T_{\text{CMB}}$	temperature at the core-mantle boundary, generally at $P \approx 40$ Mbar; see Table 1
$\beta$	dimensionless factor applied to prescribed barotrope $P = P(\beta\rho)$ to yield exact Jupiter mass; equivalent to compositional perturbation